

Chapter 12

Structural Relaxation of Oxide Compounds from the High-Pressure Phase

Hitoshi Yusa

Abstract In this chapter, several types of structural relaxation of oxide compounds from the high-pressure phase are systematically introduced in terms of high-pressure comparative crystallography. Structural relaxation of various ABO_3 compounds from the perovskite phase to the lithium niobate phase is explained in detail from rotation of the BO_6 octahedral frameworks. Depressurized amorphization of $ASiO_3$ perovskites containing large divalent cations ($A = Ba^{2+}$, Sr^{2+} , and Ca^{2+}) is elucidated by the characteristics of the hexagonal and cubic perovskite structures. The unquenchable $Rh_2O_3(II)$ phases of group-13 sesquioxides, such as Ga_2O_3 and In_2O_3 , are confirmed by both experimental and computational studies. Ab initio calculations of Y_2O_3 show that the unquenchable pressure-induced phase (A-type structure) is not the stable phase under high pressure. Knowledge about the unquenchable and/or metastable phases in recovered high-pressure products is beneficial for advanced computational materials design.

Keywords High-pressure experiments • Structural relaxation • Quenchability
Amorphization • Ab initio calculation

12.1 General

Under high pressure, typical ABO_3 oxide compounds undergo a phase transition with the coordination of the B atoms changing from tetrahedral to octahedral. For the most popular $MgSiO_3$ compounds, which are believed to be one of the most abundant constituent minerals in the Earth's mantle, the crystal structure changes from pyroxene to spinel (ringwoodite) plus stishovite, ilmenite (akimotoite), garnet (majorite), perovskite (bridgmanite), and postperovskite [1, 2]. All of the structures are quenchable, except for the postperovskite structure ($CaIrO_3$ structure) which appears under ultrahigh pressure above 140 GPa [2]. Therefore, the physical

H. Yusa (✉)

National Institute for Materials Science, Namiki 1-1, Tsukuba, Ibaraki, Japan
e-mail: YUSA.Hitoshi@nims.go.jp

© The Author(s) 2018

I. Tanaka (ed.), *Nanoinformatics*, https://doi.org/10.1007/978-981-10-7617-6_12

259

properties of most of the recovered structures can be investigated under ambient pressure. In this case, even the equilibrium phase boundary can be thermodynamically determined by measuring the enthalpy and heat capacity at ambient pressure [1, 3]. However, the high-pressure phase is not always quenchable. Because high-pressure phases tend to undergo structural relaxation during decompression, the high-pressure structures cannot be characterized from the recovered products. The structure can be elucidated by in situ X-ray observation under pressure. In particular, a synchrotron radiation X-ray source combined with a diamond anvil cell (DAC) can shed light on the real structure of the unquenchable phase under pressure.

Some high-pressure perovskites in ABO_3 compounds exhibit unquenchable phenomena during decompression to atmospheric pressure. There are two types of structure instability: conversion to perovskite-related structures and amorphization. Structural relaxation in the former case accompanies a symmetry change to a non-centrosymmetric structure, retaining the ferroelectricity. The representative example is structural relaxation from the orthorhombic perovskite structure to the lithium niobate structure. Many compounds with the lithium niobate structure have been found by high-pressure synthesis.

In other simple oxides, there are peculiar high-pressure phases in sesquioxides that revert to a lower pressure phase under room temperature. In some cases, there are definite crystallographic relationships between their lower pressure phases.

Ab initio computational studies are indispensable to confirm whether the phase appearing by structural relaxation is metastable. Recent computational studies have predicted novel materials with high-performance functionalities. In particular, a data-driven material design approach has identified many candidates for high-pressure synthetic materials. However, the predicted materials are not always realized in the recovered products because of structural relaxation during decompression. To enhance the capability of material design by computational approaches, systematic information about structure relaxation would be highly beneficial.

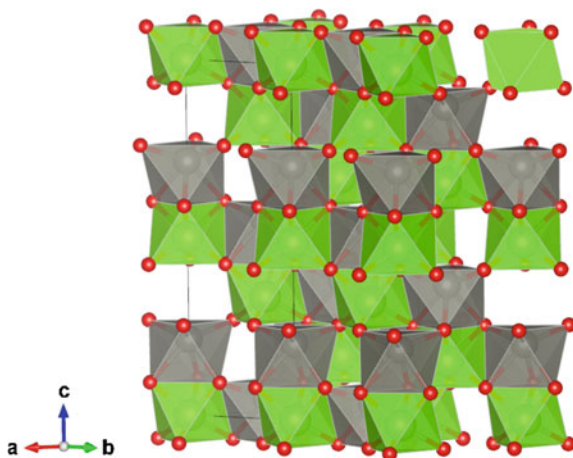
In this chapter, we focus on relaxation structure and quenchability from the high-pressure phase. By classifying the relaxation process, we discuss the recovery compounds from high-pressure synthesis.

12.2 Phase Transition from the Perovskite Structure to the Lithium Niobate Structure

12.2.1 Crystal Structure Relationship Among Lithium Niobate, Perovskite, and Ilmenite Phases

The typical lithium niobate phase of Li-bearing compounds, which is represented by $LiNbO_3$ and $LiTaO_3$, is only found in similar lithium-bearing compounds, such as $LiUO_3$ [4] and $LiReO_3$ [5], and all of these lithium niobate phases show stability

Fig. 12.1 Lithium niobate structure



under ambient conditions. In contrast, high-pressure synthesis makes it possible to crystallize lithium niobate phases of various Li-free compounds, such as $A^{2+}B^{4+}O_3$ -type [6–13] and $A^{4+}B^{2+}O_3$ -type [14] oxides. One of the lithium niobate structures is shown in Fig. 12.1. It is widely known that lithium niobate phases appear with retrogressive transition from high-pressure perovskite phases. Such a hidden perovskite phase is difficult to confirm with only the recovered high-pressure products, but it has been directly elucidated by in situ experiments under high pressure [6–9, 12–14].

It should be noted that these lithium niobate phases convert from the perovskite structure with structural relaxation during decompression, which is closely related to the rotation of BO_6 octahedra. This is a first-order transformation accompanied by a 2–3% volume change. The typical structural relationship among the ilmenite, perovskite, and lithium niobate phases is shown in Fig. 12.2. As shown in Fig. 12.2, where a specific crystallographic orientation is chosen, the transformation from lithium niobate to perovskite appears to be much easier than that from the ilmenite structure to the perovskite structure. In other words, there must be large displacement of the BO_6 octahedra to trigger the ilmenite–perovskite transition, where atomic rearrangement should be controlled by diffusion under high temperature. In fact, for many ABO_3 compounds, the perovskite to ilmenite transition is not observed at room temperature throughout the pressure range even though the density of ilmenite is smaller than that of lithium niobate.

12.2.2 Perovskite Tolerance Factor

It is believed that such instability is closely correlated with the ionic radii of the A- and B-site cations forming the perovskite structure. The Goldschmidt tolerance

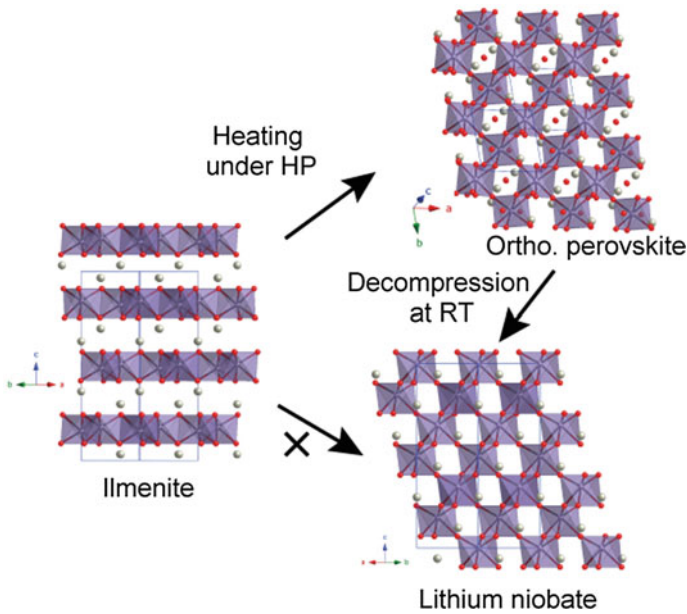


Fig. 12.2 Structural relationship among ilmenite, lithium niobate, and orthorhombic perovskite

factor [15] indicates the distortion from ideal cubic perovskite and it is also applicable to such instabilities during decompression: $t = (r_A + r_o)/\sqrt{2}(r_B + r_o)$, where r is the effective ionic radius of each element [16]. The tolerance factor is determined from the geometrical relationship of the ionic radii, as shown in Fig. 12.3. The right-hand side figures show the polyhedral types of the A-site cations. Ideal cubic perovskite ($t = 1$) is composed of cubo-octahedral coordinated A cations. Orthorhombic distortion ($t < 1$) incorporates A-site cations, forming square-antiprism-type polyhedra.

The Goldschmidt diagram is useful for understanding the degree of distortion from the ideal perovskite structure. The cation radius ratios of various ABO_3 compounds are plotted in the Goldschmidt diagram in Fig. 12.4. In Fig. 12.4, the white arrow indicates compounds in the lower right region that tend to convert to the lithium niobate phase, whereas the black arrow indicates compounds in the upper left region that tend to retain the perovskite structure. This trend means that orthorhombic distortion induces conversion to the lithium niobate phase. Orthorhombic distortion is derived from rotation of BO_6 octahedra. Therefore, rotation of BO_6 octahedra can be used to understand the degree of rotation for conversion to the lithium niobate structure. O’Keeffe et al. [17] suggested that a single rotation Φ about the triad [111] axis of a pseudocubic perovskite lattice (the direction is indicated in Fig. 12.3) can be represented as rotation of the BO_6

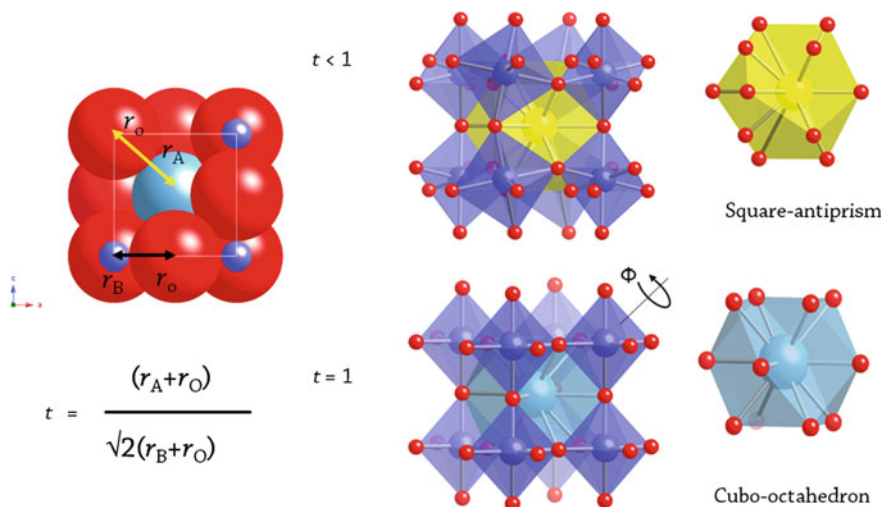
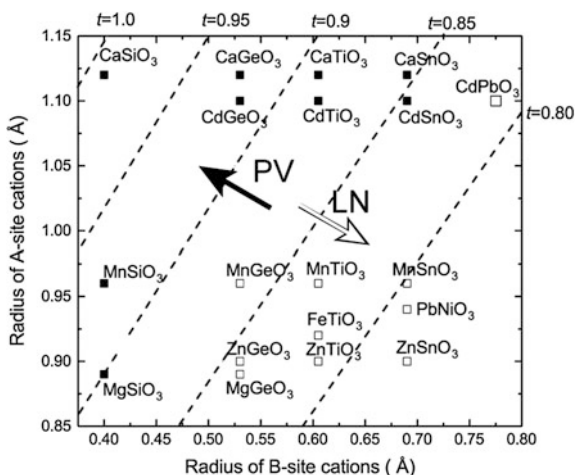


Fig. 12.3 Left: geometrical explanation of the perovskite tolerance factor. Right: orthorhombic ($t < 1$) and cubic perovskite ($t = 1$) polyhedra

Fig. 12.4 Goldschmidt diagram with tolerance factor (t) of ABO_3 compounds. The tolerance factors (dashed lines) were calculated from the ionic radii of the six-fold coordinated B cations (x axis) and eight-fold coordinated A cations (y axis). Open squares are compounds that convert to the lithium niobate structure under decompression. Solid squares are compounds that quench as the perovskite structure at ambient pressure



octahedra. The angle can be calculated from the atomic coordinates [18] or estimated from the cell dimensions: $\Phi = \cos^{-1}(\sqrt{2c^2/ab})$ [17, 19]. According to the calculated Φ values of the various perovskite compounds listed in Table 12.1, the critical angle for conversion is estimated to be 15° – 16° , except for $MgSiO_3$ perovskites. This value is useful for exploring compositions that may adopt the lithium niobate structure.

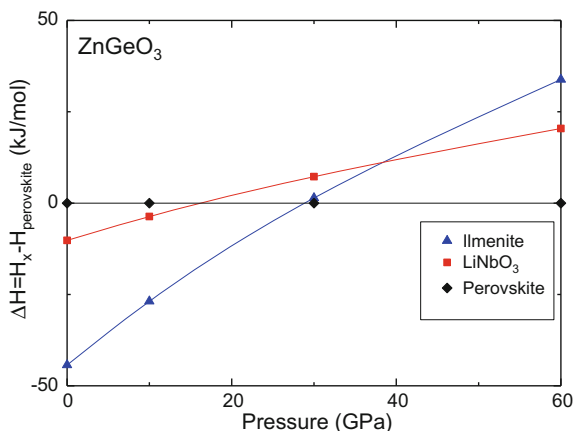
Table 12.1 Tilting angle of the BO₆ octahedra and lattice parameters of various perovskites

Compound	a (Å)	b (Å)	c (Å)	Φ (deg)	Reference
CaGeO ₃	5.2607	5.2688	7.4452	3.9	Susaki + (1983) [20]
CdGeO ₃	5.209	5.253	7.434	10.7	Susaki (1989) [21]
MnGeO ₃ (21.8 GPa)	4.9298	5.0586	7.0873	16.5	Yusa + (2014) [22]
ZnGeO ₃ (15.6 GPa)	4.8796	5.0129	7.1233	19.4	Yusa + (2006) [9]
MgGeO ₃ (17.9 GPa)	4.832	5.031	7.022	20.8	Leinenweber + (1994) [7]
CaTiO ₃	5.3796	5.4423	7.6401	10.2	Sasaki + (1987) [23]
CdTiO ₃	5.3053	5.4215	7.6176	15.5	Sasaki + (1987) [23]
MnTiO ₃ (4.45 GPa)	5.1048	5.3046	7.4180	20.5	Ross + (1989) [24]
FeTiO ₃ (16.2 GPa)	5.04	5.17	7.27	17.1	Leinenweber + (1991) [6]
(Mg, Fe)TiO ₃ (21 GPa)	4.9852	5.2104	7.2305	21.1	Linton + (1991) [8]
CdSnO ₃	5.547	5.577	7.867	7.3	Smith (1960) [25]
MnSnO ₃ (7.35 GPa)	5.301	5.445	7.690	18.4	Leinenweber + (1991) [6]
MnSiO ₃ (40 GPa)	4.7559	4.8073	6.7723	10.7	Fujino + (2009) [26]
ZnTiO ₃ (21 GPa)	4.9324	5.1148	7.2514	21.9	Akaogi + (2015) [27]
CaSnO ₃	5.5142	5.6634	7.8816	15.6	Zhao + (2004) [28]
MgSiO ₃	4.7754	4.9292	6.8969	18.4	Horiuchi + (1987) [29]
PbNiO ₃ (c.a. 1 atm)	5.358	5.463	7.705	15.3	Inaguma + (2010) [30]
CdPbO ₃ (1.4 GPa)	5.639	5.724	8.135	15.0	Yusa +, in preparation
ZnSnO ₃ (20.2 GPa)	5.1640	5.2546	7.4455	15.4	Yusa +, in preparation

12.2.3 Structure Stability from a Computational Viewpoint

Ab initio calculations provide useful information about the phase stability under high pressure. Enthalpy calculations have revealed the structural stability of the perovskite, lithium niobate, and ilmenite phases of several compounds. All of the lithium niobate phases are metastable under pressure. As an example, the relative differences of the enthalpies of the three phases of ZnGeO₃ perovskite are plotted as a function of pressure in Fig. 12.5. The lower pressure phase (the imenite structure) directly change to the perovskite structure. Therefore, we can conclude that the lithium niobate phase is a metastable structure of ZnGeO₃ [22]. Similar trends have been found for MnTiO₃ [31], MgGeO₃ [32], and ZnTiO₃ [10] by enthalpy calculations. A further transformation from the perovskite structure to the postperovskite structure has been confirmed for ZnGeO₃ [22] and MgGeO₃ [32].

Fig. 12.5 Enthalpy differences of the ilmenite (blue triangles) and lithium niobate (red squares) phases of ZnGeO_3 relative to the perovskite phase (black diamonds)



12.3 Amorphization from Cubic and Hexagonal Silicate Perovskites

12.3.1 Phase Transition Sequence of Silicate Perovskites

For a tolerance factor less than one, as represented by MgSiO_3 perovskite, the BO_6 octahedra in the perovskite structure tilts to make an allowance for the small divalent cations in the BO_6 octahedral corner-sharing framework. The tilting in perovskite has been discussed in detail by many researchers (e.g., Glazer [33]), where rotation does not disrupt the corner-sharing connectivity. As mentioned in Sect. 12.2, if rotation of the BO_6 octahedra reaches a limit, conversion to the lithium niobate phase occurs with a displacive-type phase transition. In contrast, perovskites bearing large divalent cations, which is formally expressed as a tolerance factor of greater than one (as shown in Fig. 12.6), cannot make enough space for such large cations in tilting of BO_6 octahedra. Therefore, silicate perovskites containing Ca^{2+} , Sr^{2+} , and Ba^{2+} cations are stabilized as hexagonal and/or cubic forms under high pressure [34–38]. These transformations have been confirmed by high-pressure experiments. The phase transition sequence is summarized in Table 12.2.

12.3.2 Crystal Structures of Hexagonal Perovskite and Structural Relation with Cubic Perovskite

Perovskites containing large divalent cations tend to expand and form a BO_6 face-sharing octahedral framework to accommodate the large cations, where the B^{4+} ions in the face-sharing octahedra cause oxygen anions to move to closer to

Fig. 12.6 Goldschmidt diagram with tolerance factor (t) for ABO_3 compounds. The solid line indicates $t = 1$. The tolerance factors were calculated from the ionic radii of the six-fold coordinated B cations (x axis) and eight-fold coordinated A cations (y axis). Open diamonds are compounds that convert to the amorphous form under decompression. Solid and open squares are compounds that quench as the perovskite structure and convert to the lithium niobate structure at ambient pressure, respectively

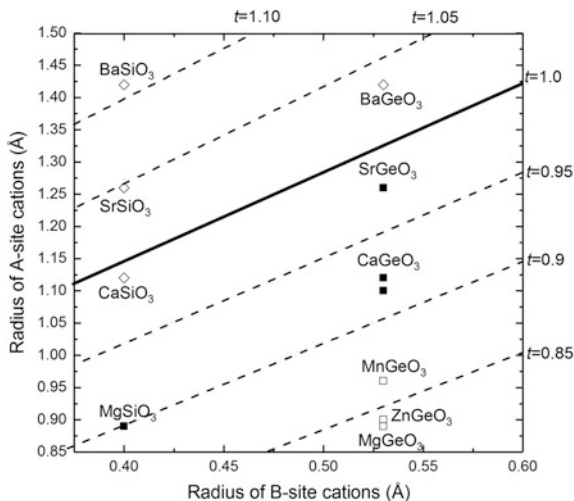


Table 12.2 High-pressure phase transition sequences of $ASiO_3$ ($A = Ca, Sr,$ and Ba) and transition pressures

$CaSiO_3$	$SrSiO_3$	$BaSiO_3$
wollastonite [39]	pseudowollastonite [40]	High-T $BaGeO_3$ type [41]
~3 GPa	~4 GPa	~4 GPa
walstromite [39, 42]	walstromite [43]	$BaSiO_3(II)$ [44]
~9 GPa	~9 GPa	~12 GPa
$Ca_2SiO_4 + CaSi_2O_5$ [42]	$Sr_2SiO_4 + SrSi_2O_5$ [36, 45]	$Ba_2SiO_4 + BaSi_2O_5$ [37]
~13 GPa	~20 GPa	~18 GPa
cubic perovskite [34]	6H perovskite [35]	9R perovskite [37]
	~38 GPa	~40 GPa
	cubic perovskite [38]	6H perovskite [37]
		~140 GPa
		cubic perovskite [46]

reduce their repulsion. Stacking of the face-sharing framework in the c -axis direction results in a hexagonal unit cell. Examples of the hexagonal crystal structures of $BaSiO_3$ [37] are shown in Fig. 12.7.

In Fig. 12.7, both the SiO_6 octahedra and barium atoms are shown along the c -axis direction to clarify the relationships of the stacking sequences. The 9R phase (space group $R\bar{3}m$) resembles the 6H phase (space group $P6_3/mmc$) in that the SiO_6 octahedra are periodically connected by face sharing. The difference is the periodicity of the face- and corner-sharing of SiO_6 octahedra. In the c -axis direction, 9R perovskite exhibits a $(chh)_3$ sequence whereas 6H perovskite exhibits a $(cch)_2$ sequence, where c and h correspond to corner- and face-sharing octahedra, respectively. For perovskites, It is known that such hexagonal polytypes lie in a

sequence from 9R to 3C (space group $R\bar{3}m$) cubic perovskites. In this hexagonal sequence, pressure increases the frequency of corner-sharing octahedra. This relation can be extended to cubic perovskite (3C), which only consist of corner-sharing octahedral, as shown in Fig. 12.8. For BaSiO_3 , the density increases for the transitions from 9R to 6H and 6H to 3C are 3.5% and 1.4%, respectively.

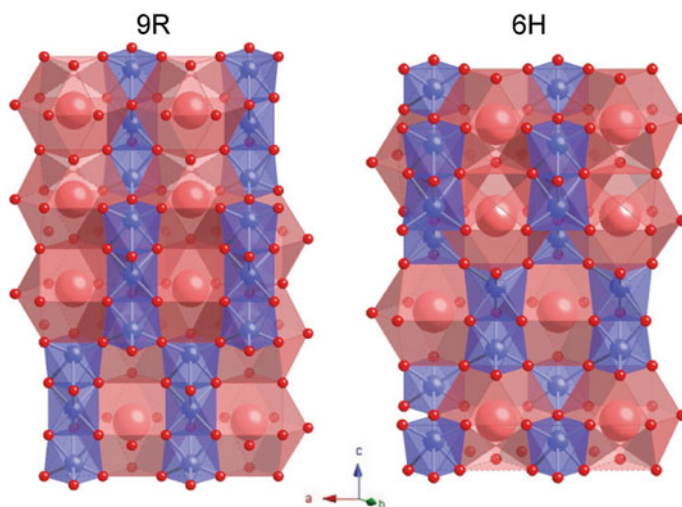


Fig. 12.7 Crystal structures of 9R and 6H BaSiO_3

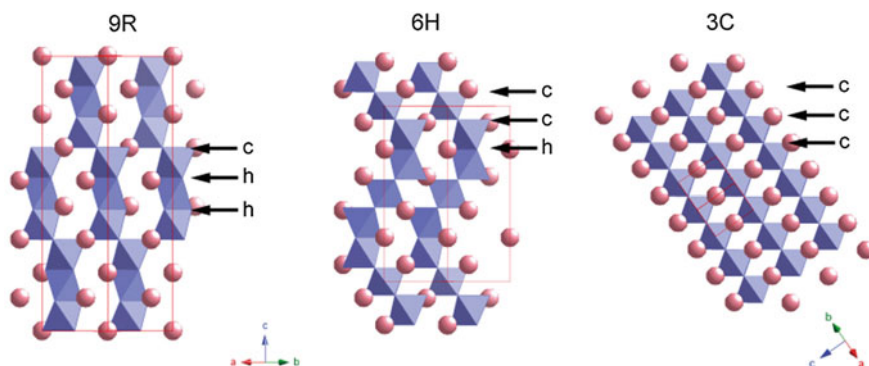


Fig. 12.8 Structural relationship among 9R, 6H, and 3C perovskites in terms of the BO_6 stacking sequence

12.3.3 Phase Diagrams: Experiments and Ab Initio Calculations

The ionic radius can be controlled under high pressure. In particular, larger A-site cations in perovskites, such as Sr^{2+} and Ba^{2+} , are sensitive to pressure. The A-site cations are compressed to SiO_6 octahedra and the face-sharing octahedral frequency then gradually decreases with increasing pressure. Furthermore, as shown in the phase diagram based on high-pressure experiments in Fig. 12.9, for cubic perovskites, there is a systematic relation between the transition pressure and the A^{2+} radius. For the BaSiO_3 compound, the transition occurs above 130 GPa [46]. In contrast, the transitions of the cubic perovskites CaSiO_3 and SrSiO_3 occur at significantly lower pressures of 15 and 38 GPa, respectively. Note that SrSiO_3 does not transform to a 9R-type hexagonal perovskite, such as that of BaSiO_3 . Furthermore, no hexagonal perovskites are found for CaSiO_3 . These results can be simply explained by the difference of the cation radii in the A sites.

Figure 12.10 shows the phase diagram of BaSiO_3 at 0 K from ab initio calculations [46]. The phase transition sequence is consistent with that from high-pressure experiments, although the calculated transition pressures are underestimated.

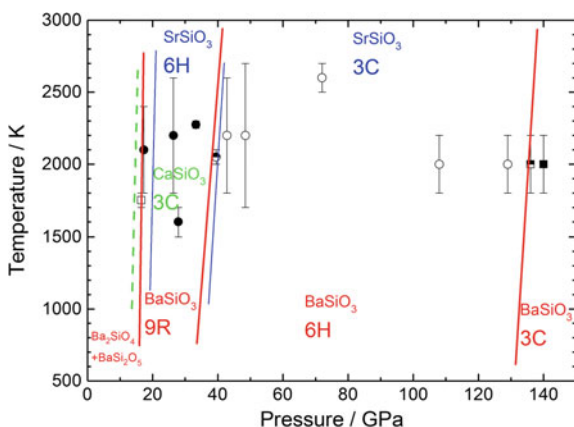
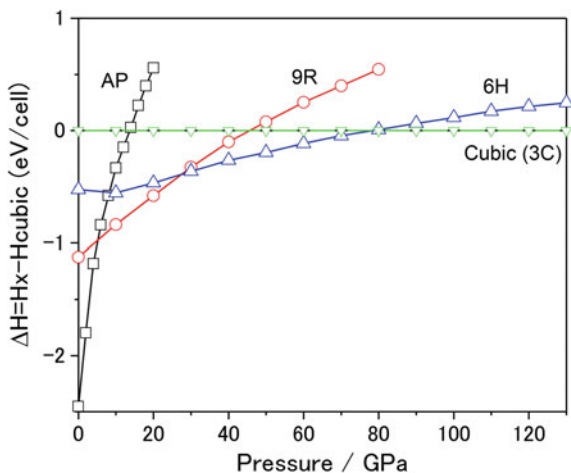


Fig. 12.9 Phase diagram of BaSiO_3 estimated from data plots of high pressure–high temperature experiments using a laser-heated DAC. Solid circles, open circles, and solid squares represent 9R, 6H, and 3C perovskites, respectively. Half-filled symbols indicate a phase mixture. The open square symbol at low pressure represents phase disproportionation of $\text{Ba}_2\text{SiO}_4 + \text{BaSi}_2\text{O}_5$. The estimated phase boundaries of BaSiO_3 (red solid lines), SrSiO_3 (blue thin lines), and CaSiO_3 (green broken line) are indicated for comparison

Fig. 12.10 Relative enthalpy differences of the BaSiO_3 phases [46] as a function of pressure. AP represents an ambient phase



12.3.4 Amorphization Under Decompression at Room Temperature

In the cubic and hexagonal perovskites stabilized under high pressure, the A-site cations are compressed to retain the BO_6 framework structure. In other words, the cations expand under decompression. Among the high-pressure phases of silicate perovskites, the first reported example was amorphization of CaSiO_3 perovskite, which was confirmed at a pressure very close to 1 atm. Because the ambient wollastonite phase is composed of a SiO_4 tetrahedral chain structure, the cubic perovskite structure cannot revert to the ambient structure at room temperature. The corner-sharing BO_6 framework can be adjusted for smaller cations, as suggested by conversion to the lithium niobate structure. However, the framework is not as flexible for larger cations. Therefore, expansion of the A-site cations disrupts the framework and makes the structure amorphous. Amorphization of the cubic perovskite structure has also been observed for SrSiO_3 [38] and BaSiO_3 [46]. Considering the structural similarity, the hexagonal perovskite structures could become amorphous during decompression. The pressure for amorphization is believed to be related to the A-site cation size in the hexagonal perovskites because the BO_6 face-sharing frequency of hexagonal perovskites is correlated with the cation size. The experimental results for BaSiO_3 are shown in Fig. 12.11. The 6H phase begins to decompose at 21.9 GPa. In contrast, the 9R phase persists at 8.9 GPa and suddenly changes to amorphous at 4.8 GPa. At 1.8 GPa, both of the phases completely change to amorphous. As a result, we can conclude that the stability of 9R is higher than that of 6H. However, this type of amorphization has not been elucidated by computational approaches. If the ionic radii are determined under pressure, this type of structural instability related to amorphization could be clarified.

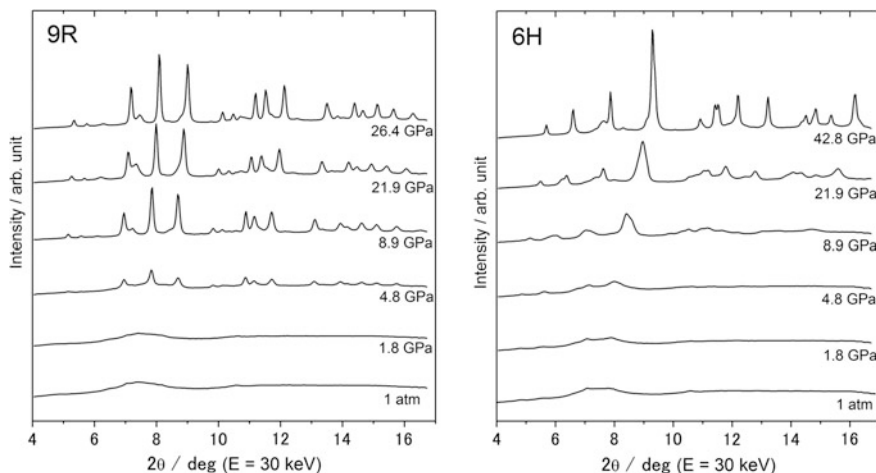


Fig. 12.11 In situ X-ray diffraction profiles of the 9R and 6H perovskites of BaSiO_3 during decompression

12.4 Relaxation Structures from the High-Pressure Phases of Sesquioxides

12.4.1 $\text{Rh}_2\text{O}_3(\text{II})$ Structure Reverting to the Corundum Structure in Group 13 Sesquioxides

Group-13 sesquioxides, such as aluminum oxide, gallium oxide, and indium oxide, have been widely investigated as attractive electroceramics. Their most stable phases under ambient conditions, corundum (Al_2O_3), monoclinic $\beta\text{-Ga}_2\text{O}_3$, and cubic In_2O_3 (bixbyite-type structure, C-type rare earth sesquioxide structure, hereafter denoted as C-RES), are used for many application, such as lasers and transparent electronic devices [47, 48]. It is believed that their dense phase is the corundum structure [49]. However, in situ X-ray diffraction experiments have revealed that the $\text{Rh}_2\text{O}_3(\text{II})$ structure that appears as a post-corundum phase under pressure reverts to the corundum structure under decompression. In Al_2O_3 , the corundum structure that transforms to the $\text{Rh}_2\text{O}_3(\text{II})$ phase under very high pressure above 95 GPa reverts to the corundum structure at ambient pressure after decompression [50, 51]. In other instances, the $\text{Rh}_2\text{O}_3(\text{II})$ phase in Ga_2O_3 identified under pressure transforms to the corundum phase after decompression rather than changing to $\beta\text{-Ga}_2\text{O}_3$ [52], as shown in Fig. 12.12.

Figure 12.13 shows the crystal structures of the $\text{Rh}_2\text{O}_3(\text{II})$ -type and corundum structures of Ga_2O_3 with a specific direction for comparison. A twin-like relation between the $\text{Rh}_2\text{O}_3(\text{II})$ and corundum phases can be seen in the vertical direction. Considering the structural resemblance between $\text{Rh}_2\text{O}_3(\text{II})$ and corundum, we

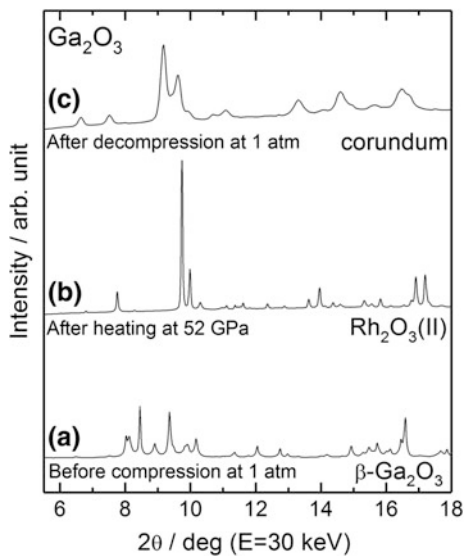


Fig. 12.12 X-ray diffraction profiles of Ga_2O_3 samples. **a** Starting $\beta\text{-Ga}_2\text{O}_3$ structure at ambient pressure, **b** $\text{Rh}_2\text{O}_3(\text{II})$ structure after laser heating at 52 GPa, and **c** corundum structure after decompression at ambient pressure

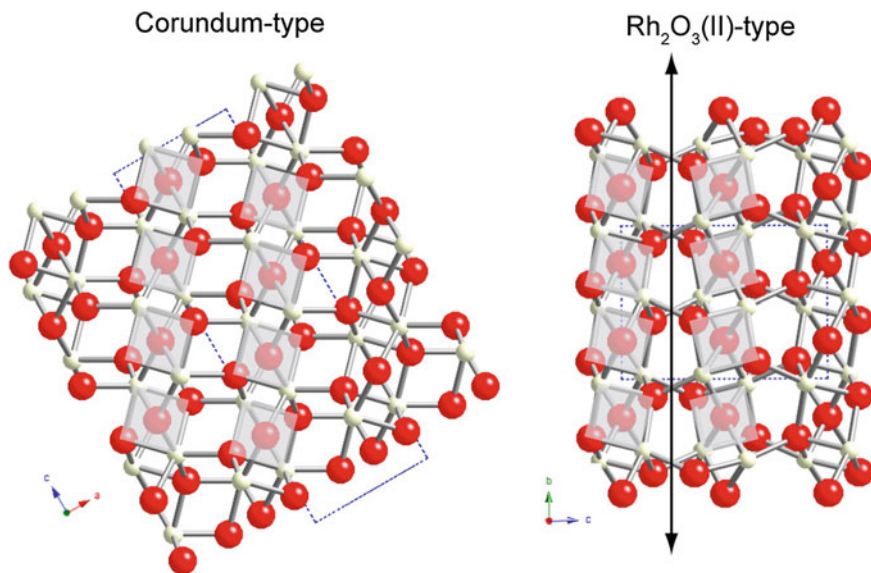


Fig. 12.13 Projections of the corundum structure of Ga_2O_3 along the hexagonal a axis (left) and the $\text{Rh}_2\text{O}_3(\text{II})$ structure of Ga_2O_3 along the a axis (right)

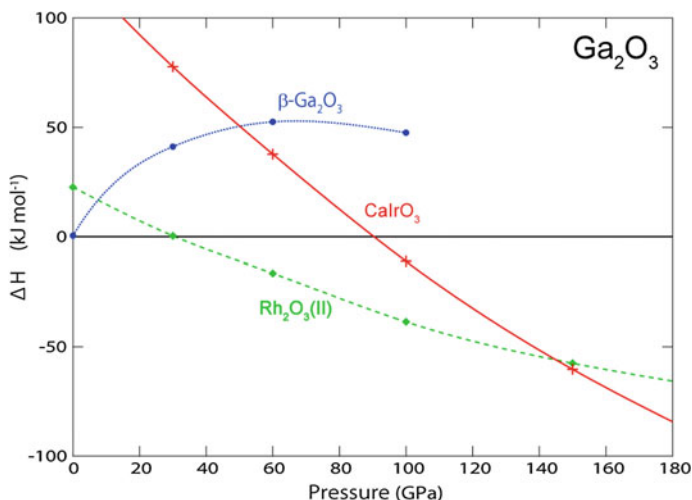


Fig. 12.14 Enthalpies of the Ga_2O_3 polymorphs relative to the corundum structure: $\beta\text{-Ga}_2\text{O}_3$ (blue circles), $\text{Rh}_2\text{O}_3(\text{II})$ (green diamonds), and CaIrO_3 (red crosses)

conclude that the $\text{Rh}_2\text{O}_3(\text{II})$ structure is appropriate for the post-corundum phase of Ga_2O_3 .

The differences in the static enthalpies of $\beta\text{-Ga}_2\text{O}_3$ and $\text{Rh}_2\text{O}_3(\text{II})$ -type Ga_2O_3 relative to corundum-type Ga_2O_3 calculated by density functional theory (DFT) with the local density approximation (LDA) are shown in Fig. 12.14. The transitions from $\beta\text{-Ga}_2\text{O}_3$ to corundum-type Ga_2O_3 and corundum-type Ga_2O_3 to $\text{Rh}_2\text{O}_3(\text{II})$ -type Ga_2O_3 occur at about 0 and 30 GPa, respectively [52]. According to further phase investigation, the stability field continues to 130 GPa until the CaIrO_3 -type structure appears [53].

For In_2O_3 , in situ X-ray experiments reveal that the stability region for corundum phase is very narrow because the single corundum phase is not observed at any pressure [52]. This is consistent with the calculated results, which suggest the absence of a stability area for the corundum phase (Fig. 12.15) [52]. However, the recovered phase after decompression exhibits the corundum phase. Therefore, it can be concluded that the corundum phase appearing in the recovered sample is converted from the $\text{Rh}_2\text{O}_3(\text{II})$ phase. The volume change from the $\text{Rh}_2\text{O}_3(\text{II})$ phase to the corundum phase is estimated to be 2.1%, which is comparable with the changes of 3.1% for Al_2O_3 [51] and 2.3% for Ga_2O_3 . The $\text{Rh}_2\text{O}_3(\text{II})$ phase does not transform to the CaIrO_3 structure, which had been predicted by a computational study [54]. Instead, a more dense and higher coordinated phase with the Gd_2S_3 -type structure has been confirmed at about 40 GPa from an experimental and computational study [55]. The enthalpy relations from DFT calculations are shown in Fig. 12.15.

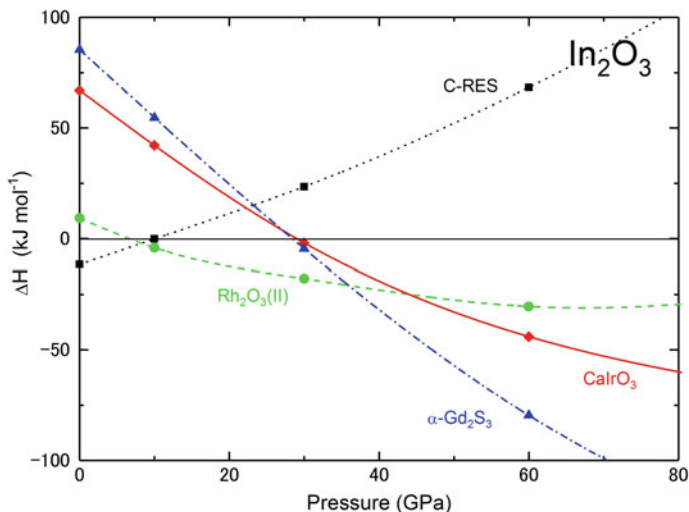


Fig. 12.15 Enthalpies of the In_2O_3 polymorphs relative to the corundum structure: C-RES (black squares), $\text{Rh}_2\text{O}_3(\text{II})$ (green circles), Gd_2S_3 (blue triangles), and CaIrO_3 (red diamonds)

12.4.2 A-RES Structure of Y_2O_3 Reverting to the B-RES Structure

Yttrium has a similar ionic radius to the ionic radii of lanthanides, so lanthanide ions can be incorporated into yttria to make optical ceramics, such as $\text{Eu}^{3+}:\text{Y}_2\text{O}_3$ phosphor [56] and $\text{Yb}^{3+}:\text{Y}_2\text{O}_3$ laser [57]. Yttria crystallizes in the bixbyite structure (C-RES) under ambient conditions, similar to lanthanide sesquioxides. B-RES has been confirmed as the high-pressure phase in the recovery sample from high-pressure experiments. The A-RES phase was not found, which is expected to be part of the phase transformation sequence of lanthanide sesquioxides [58]. In situ X-ray diffraction experiments performed at room temperature using a DAC revealed the existence of the A-RES phase [59]. Back transformation to the B-RES structure was also confirmed. The reversible transformation mechanism from B-RES to A-RES can be explained from a crystallographic viewpoint, as shown in Fig. 12.16.

The B-RES structure of yttria consists of three different yttrium sites. Among these sites, only the Y3 site can be considered to possess six-fold oxygen coordination because the Y3–O2 distance is too long to be classified as seven-fold coordination, as shown in Fig. 12.16b. With increasing pressure, O2 moves closer to Y3, which results in the formation of seven-fold polyhedra. Upon further compression to 15–20 GPa, the Y3–O2 distance becomes shorter than the average Y3–O distance. The B-RES structure finally changes to the structure shown in Fig. 12.16c, which is equivalent to the A-RES structure. This means that the A-RES structure can be directly derived from the B-RES structure. The volume

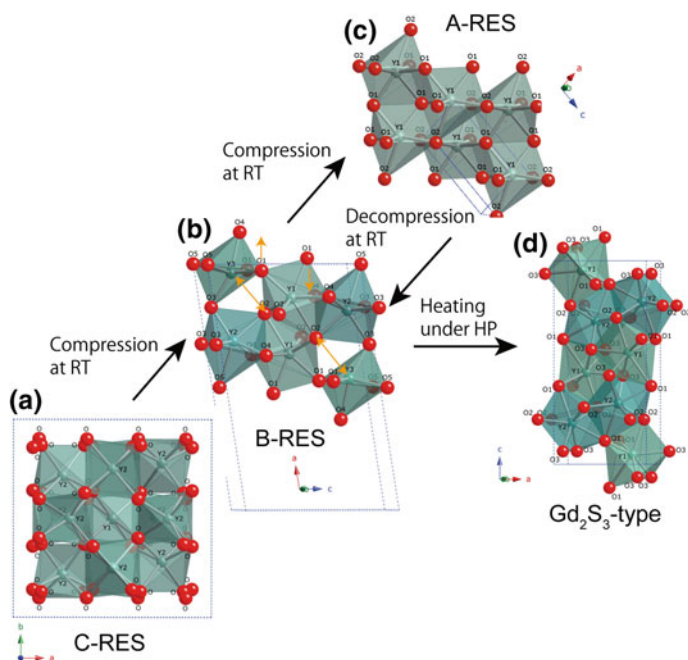


Fig. 12.16 Structural relationship among the high-pressure polymorphs of Y_2O_3

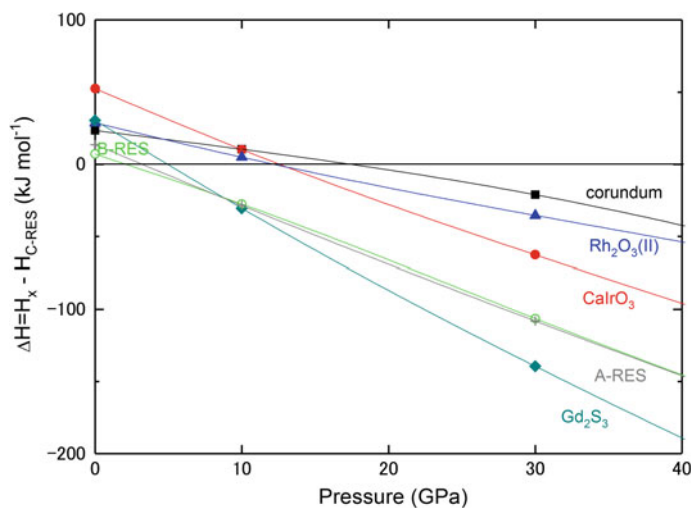


Fig. 12.17 Enthalpies of the Y_2O_3 polymorphs relative to the C-RES structure: B-RES (open green circles), A-RES (green crosses), Gd_2S_3 (green diamonds), CaIrO_3 (red circles), $\text{Rh}_2\text{O}_3(\text{II})$ (blue triangles), and corundum (black squares)

change from the B-RES structure to the A-RES structure (2.5%) is characteristic of a first-order phase transition.

Contrary to confirmation of the A-RES structure by compression experiments at room temperature, enthalpy calculations performed by DFT with the LDA indicate no stability region of the A-RES structure (Fig. 12.17) [59]. The transition to the other high-coordination structure (Gd_2S_3 -type structure, Fig. 12.16d) occurs before the appearance of the A-RES phase. In fact, laser heating experiments under high pressure result in Y_2O_3 crystallizing in the Gd_2S_3 structure at about 10 GPa. Therefore, it can be concluded that the A-RES structure appearing under room temperature compression is a metastable phase.

12.5 Concluding Remarks

Large volume high-pressure apparatus (e.g., cubic, belt, and KAWAI-type presses) is a fundamental tool for materials scientists, because high-pressure methods enable the synthesis of novel materials under ambient conditions. High-pressure synthesis provides the opportunity to obtain high density and/or highly coordinated compounds. However, the recovered product does not always reflect the structure under pressure. If a new structure is found, the stability relation with the lower pressure phase(s) should be evaluated using computational approaches, such as *ab initio* calculations. If the structure is a metastable phase, the structure should be examined for crystallographic similarity with an objective structure. Conversion to the metastable phase would be clarified by structural relaxation. A trace amount of a high-pressure phase is sometimes found in the recovered products as a defect origination from twin structures. This is also an indication to identify the unquenchable high-pressure phase.

In situ X-ray diffraction is the most powerful approach to determine structures under pressure. In some cases, recompression of the metastable phase gives the high-pressure structure. During structural relaxation, symmetry change likely occurs, as exemplified by the transition from the perovskite to the lithium niobate phase as described in Sect. 12.2. Relaxation from a centrosymmetric to a non-centrosymmetric structure is important to determine the functionality, such as ferroelectricity.

As mentioned in Sect. 12.3, amorphization is a usual phenomenon for high-pressure products under decompression. Therefore, if there is a complete or part of an amorphous-like pattern in the X-ray diffraction profile of the recovered product, the amorphous structure is an indication of an unquenchable high-pressure phase. In situ X-ray experiments using a laser-heated DAC reveal the structure of the unquenchable phase. Amorphization can be triggered by the expansion of specific cations during decompression. In particular, elucidation of the compression behavior for relatively large cations, such as K^+ , Ca^{2+} , Sr^{2+} , and Ba^{2+} , would aid in understanding the quenchability of high-pressure structures containing such cations. Therefore, an approach to determine the ionic radii under pressure is required for prediction of the quenchability.

Acknowledgements I am deeply grateful to Prof. I. Tanaka and Dr. T. Taniguchi for their advice on the topics discussed in this chapter. I thank Profs. T. Tsuchiya and H. Hiramatsu for discussion on the computational studies. The X-ray diffraction experiments were performed under SPRING-8 and KEK proposals. This work was supported in part by Innovative Areas “Nano Informatics” (Grant No. 25106006) and JSPS KAKENHI (Grant No. 16H04078).

References

1. H. Yusa, M. Akaogi, E. Ito, *J. Geophys. Res.-Solid Earth* **98**, 6453 (1993)
2. M. Murakami, K. Hirose, K. Kawamura, N. Sata, Y. Ohishi, *Science* **304**, 855 (2004)
3. M. Akaogi, E. Ito, *Geophys. Res. Lett.* **20**, 1839 (1993)
4. Y. Hinatsu, T. Fujino, N. Edelstein, *J. Solid State Chem.* **99**, 182 (1992)
5. R.J. Cava, A. Santoro, D.W. Murphy, S. Zahurak, R.S. Roth, *J. Solid State Chem.* **42**, 251 (1982)
6. K. Leinenweber, W. Utsumi, Y. Tsuchida, T. Yagi, K. Kurita, *Phys. Chem. Miner.* **18**, 244 (1991)
7. K. Leinenweber, Y.B. Wang, T. Yagi, H. Yusa, *Am. Mineral.* **79**, 197 (1994)
8. J.A. Linton, Y.W. Fei, A. Navrotsky, *Am. Mineral.* **84**, 1595 (1999)
9. H. Yusa, M. Akaogi, N. Sata, H. Kojitani, R. Yamamoto, Y. Ohishi, *Phys. Chem. Miner.* **33**, 217 (2006)
10. Y. Inaguma, A. Aimi, Y. Shirako, D. Sakurai, D. Mori, H. Kojitani, M. Akaogi, M. Nakayama, *J. Am. Chem. Soc.* **136**, 2748 (2014)
11. Y. Inaguma, M. Yoshida, T. Tsuchiya, A. Aimi, K. Tanaka, T. Katsumata, D. Mori, *J. Phys.: Conf. Ser.* **215**, 012131 (2010)
12. T. Hattori, T. Matsuda, T. Tsuchiya, T. Nagai, T. Yamanaka, *Phys. Chem. Miner.* **26**, 212 (1999)
13. W. Wang, S. Wang, D. He, J.A. Xu, *Solid State Commun.* **196**, 8 (2014)
14. Y. Inaguma, K. Tanaka, T. Tsuchiya, D. Mori, T. Katsumata, T. Ohba, K.-I. Hiraki, T. Takahashi, H. Saitoh, *J. Am. Chem. Soc.* **133**, 16920 (2011)
15. V.M. Goldschmidt, *Naturwissenschaften* **14**, 477 (1926)
16. R.D. Shannon, *Acta Crystallographica Section A* **32**, 751 (1976)
17. M. O'keeffe, B.G. Hyde, J.O. Bovin, *Phys. Chem. Miner.* **4**, 299 (1979)
18. Y. Zhao, D.J. Weidner, J.B. Parise, D.E. Cox, *Phys. Earth Planet. Inter.* **76**, 17 (1993)
19. Y. Zhao, D.J. Weidner, J.B. Parise, D.E. Cox, *Phys. Earth Planet. Inter.* **76**, 1 (1993)
20. S. Sasaki, C.T. Prewitt, R.C. Liebermann, *Am. Mineral.* **68**, 1189 (1983)
21. J. Susaki, *Phys. Chem. Miner.* **16**, 634 (1989)
22. H. Yusa, T. Tsuchiya, M. Akaogi, H. Kojitani, D. Yamazaki, N. Hirao, Y. Ohishi, T. Kikegawa, *Inorg. Chem.* **53**, 11732 (2014)
23. S. Sasaki, C.T. Prewitt, J.D. Bass, W.A. Schulze, *Acta Crystallogr. Sect. C-Struct. Chem.* **43**, 1668 (1987)
24. N.L. Ross, J.D. Ko, C.T. Prewitt, *Phys. Chem. Miner.* **16**, 621 (1989)
25. A. Smith, *Acta Crystallogr.* **13**, 749 (1960)
26. K. Fujino, D. Nishio-Hamane, K. Suzuki, H. Izumi, Y. Seto, T. Nagai, *Phys. Earth Planet. Inter.* **177**, 147 (2009)
27. M. Akaogi, K. Abe, H. Yusa, H. Kojitani, D. Mori, Y. Inaguma, *Phys. Chem. Miner.* **42**, 421 (2015)
28. J. Zhao, N.L. Ross, R.J. Angel, *Phys. Chem. Miner.* **31**, 299 (2004)
29. H. Horiuchi, E. Ito, D.J. Weidner, *Am. Mineral.* **72**, 357 (1987)
30. Y. Inaguma, M. Yoshida, T. Tsuchiya, A. Aimi, K. Tanaka, T. Katsumata, D. Mori, *J. Phys.: Conf. Ser.* **215**, 012131 (2010)
31. F. Zhu, X. Wu, S. Qin, *Solid State Commun.* **152**, 984 (2012)

32. T. Tsuchiya, J. Tsuchiya, *Phys. Rev. B* **76**, 092105 (2007)
33. A.M. Glazer, M. Ahtee, H.D. Megaw, *Acta Crystallogr. Sect. A* **28**, S179 (1972)
34. H.K. Mao, L.C. Chen, R.J. Hemley, A.P. Jephcoat, Y. Wu, W.A. Bassett, *J. Geophys. Res.-Solid Earth Planets* **94**, 17889 (1989)
35. H. Yusa, M. Akaogi, N. Sata, H. Kojitani, Y. Kato, Y. Ohishi, *Am. Mineral.* **90**, 1017 (2005)
36. M. Akaogi, H. Kojitani, H. Yusa, R. Yamamoto, M. Kido, K. Koyama, *Phys. Chem. Miner.* **32**, 603 (2005)
37. H. Yusa, N. Sata, Y. Ohishi, *Am. Mineral.* **92**, 648 (2007)
38. W.S. Xiao, D.Y. Tan, W. Zhou, J. Liu, J. Xu, *Am. Mineral.* **98**, 2096 (2013)
39. T. Gasparik, K. Wolf, C.M. Smith, *Am. Mineral.* **79**, 1219 (1994)
40. F. Nishi, *Acta Crystallogr. Sect. C-Cryst. Struct. Commun.* **53**, 534 (1997)
41. W. Hilmer, *Acta Crystallogr* **15**, 1101 (1962)
42. M. Akaogi, M. Yano, Y. Tejima, M. Iijima, H. Kojitani, *Phys. Earth Planet. Inter.* **143**, 145 (2004)
43. K. Machida, G. Adachi, J. Shiokawa, M. Shimada, M. Koizumi, K. Suito, A. Onodera, *Inorg. Chem.* **21**, 1512 (1982)
44. Y. Shimizu, Y. Syono, S. Akimoto, *High Temperatures-High Pressures* **2**, 113 (1970)
45. H. Kojitani, M. Kido, M. Akaogi, *Phys. Chem. Miner.* **32**, 290 (2005)
46. H. Hiramatsu, Y. Hitoshi, I. Ryo, O. Yasuo, T. Kamiya, H. Hosono, *Inorg. Chem.* **56** (2017)
47. K. Matsuzaki, H. Yanagi, T. Kamiya, H. Hiramatsu, K. Nomura, M. Hirano, H. Hosono, *Appl. Phys. Lett.* **88**, 092106 (2006)
48. H. Ohta, K. Nomura, H. Hiramatsu, K. Ueda, T. Kamiya, M. Hirano, H. Hosono, *Solid-State Electron.* **47**, 2261 (2003)
49. C.T. Prewitt, R.D. Shannon, D.B. Rogers, A.W. Sleight, *Inorg. Chem.* **8**, 1985 (1969)
50. N. Funamori, R. Jeanloz, *Science* **278**, 1109 (1997)
51. J.F. Lin, O. Degtyareva, C.T. Prewitt, P. Dera, N. Sata, E. Gregoryanz, H.K. Mao, R. J. Hemley, *Nat. Mater.* **3**, 389 (2004)
52. H. Yusa, T. Tsuchiya, N. Sata, Y. Ohishi, *Phys. Rev. B* **77** (2008)
53. T. Tsuchiya, H. Yusa, J. Tsuchiya, *Phys. Rev. B* **76** (2007)
54. R. Caracas, R.E. Cohen, *Phys. Rev. B* **76**, 184101 (2007)
55. H. Yusa, T. Tsuchiya, J. Tsuchiya, N. Sata, Y. Ohishi, *Phys. Rev. B* **78** (2008)
56. S.L. Jones, D. Kumar, R.K. Singh, P.H. Holloway, *Appl. Phys. Lett.* **71**, 404 (1997)
57. J. Kong et al., *Appl. Phys. Lett.* **82**, 2556 (2003)
58. V.M.U. Goldschmidt, F. Barth, T.S.k.R, Nor, *V. Akad. Kl. 1: Mat. Naturvindensk.* **5** (1925)
59. H. Yusa, T. Tsuchiya, N. Sata, Y. Ohishi, *Inorg. Chem.* **49**, 4478 (2010)

Open Access This chapter is licensed under the terms of the Creative Commons Attribution 4.0 International License (<http://creativecommons.org/licenses/by/4.0/>), which permits use, sharing, adaptation, distribution and reproduction in any medium or format, as long as you give appropriate credit to the original author(s) and the source, provide a link to the Creative Commons license and indicate if changes were made.

The images or other third party material in this chapter are included in the chapter's Creative Commons license, unless indicated otherwise in a credit line to the material. If material is not included in the chapter's Creative Commons license and your intended use is not permitted by statutory regulation or exceeds the permitted use, you will need to obtain permission directly from the copyright holder.

